Polarimetric SAR Imaging for Extended Targets in Clutter

Kaitlyn Voccola
Air Force Research Laboratory
Sensors Directorate RYAP
Email: kaitlyn.voccola.ctr@wpafb.af.mil

Margaret Cheney
Rensselaer Polytechnic Institute
Department of Mathematical Sciences
Email: cheney@rpi.edu

Birsen Yazici
Rensselaer Polytechnic Institute
Department of Electrical, Computer, & Systems Engineering
Email: yazici@esce.rpi.edu

***Abstract*— This paper presents an analytic inversion scheme for polarimetric synthetic-aperture radar in the case of an extended target embedded in clutter and thermal noise. We developed a filtered-backprojection-type reconstruction method. We model targets and clutter as collections of dipoles, so that in each pixel we reconstruct a scattering matrix. In addition, we implement directional scattering assumptions for the curve-like extended target. For the inversion we choose to find the filter which minimizes the mean-square error between the reconstructed image and the actual target scattering matrix. Our work differs from standard polarimetric SAR imaging in that we do not perform channel-by-channel image reconstruction. We find that it is preferable to use a coupled reconstruction scheme in which we use all sets of collected data to form each element of the scattering matrix. We show in our numerical experiments that the coupled technique not only minimizes the mean-square error, but also increases the image signal-to-clutter ratio.**

I. Introduction

In synthetic-aperture radar (SAR) imaging, a moving antenna transmits electromagnetic waves that illuminate a scene. The scattered waves are measured by the same or another antenna, and from these measurements we reconstruct an image of the scene.

This paper focuses on the extension of a hybrid SAR reconstruction technique that uses both analytical and statistical theory in the framework of backprojection. This technique was previously developed for the scalar case in [15]. This work showed that incorporating the statistics of the scene into the imaging algorithm leads to clutter mitigation and also minimizes the effect of noise on the image. We extend these results to a full vector treatment of the transmission and scattering of the electromagnetic waves. That is, we consider the case when a fully polarimetric radar system is used.

Polarimetric radar has the advantage of producing multiple sets of data during a single data collection. It therefore provides more information for the image reconstruction task. It has not been convincingly demonstrated, however, that this extra information actually improves image quality sufficiently to justify the additional hardware and computational cost of using a polarimetric system. We present a technique that gives quantifiable improvements in image quality, namely reduced mean-square error (MSE) and improved image signal-to-clutter ratio (SCR).

We note that most work in polarimetry has focused solely on detection and estimation schemes [9], [5], [6], [10], [11], [12], [8]. It is typically assumed that one can reconstruct each element of the target scattering matrix from the corresponding data set. Therefore standard imaging schemes are applied to each set of data separately. Our analysis, however, shows that it is better to use instead a coupled image reconstruction technique. We stress that our work differs significantly from most work in polarimetry. We do not assume that we already have an accurate estimate of the scattering matrix and then attempt to perform target decomposition as most researchers do in polarimetry [9]. We instead begin with Maxwell's equations and re-derive the forward scattering model and develop a novel reconstruction, or estimation, of the scattering matrix. The coupled reconstruction uses every data set to reconstruct each element of the target scattering matrix. This adds to the computation time of the imaging algorithm but we show that this improves the MSE and image SCR as stated above. Moreover, this algorithm enables one to reconstruct target orientation correctly even when typical polarimetric imaging fails.

In developing this polarimetric imaging scheme we consider specifically extended targets embedded in clutter. These extended targets are anisotropic scatterers, in the sense that they scatter electromagnetic waves differently in different directions. Most man-made objects scatter anisotropically. For simplicity we consider the case of an edge or curve, although this work may be extended for more complicated targets. The examples presented here are for linear curves. For the sake of space we did not include curves with varying orientation, however the method appears to give promising results in this case as well.

Anisotropic scattering has been studied previously by many researchers [1], [7]. For example, in [1] the radar data is broken up into data from different sets of observation angles, or different frequency sub-bands. This does provide information about the directional nature of the scattering, but it leads to a reduction in resolution, because the data is processed over smaller apertures or smaller bandwidths.

We instead choose to incorporate the anisotropic scattering behavior into the target model. We assume that scatterers in the scene are made up of dipole scattering elements. Such dipole scatterers have an orientation and a location, and they display anisotropic scattering behavior. This dipole scattering model was previously considered in [7]. Our work differs from [7] in

978-1-4673-0658-4/12/$31.00 ©2012 IEEE

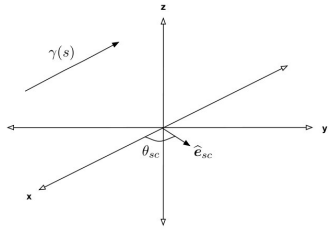

Fig. 1. Target-centered coordinate system

that we make simplifying assumptions that allow us to write out an analytic formula for the image reconstruction. The work [7], on the other hand, focuses on a purely numerical solution.

The remainder of the paper is organized as follows. In the next section we derive the forward model. We then discuss the scheme of backprojection and define our imaging operator. We include in this section results giving the optimal filter in the mean-square sense for the case when the target and clutter are statistically independent. Finally we include numerical simulations demonstrating the results of our coupled imaging scheme and compare with standard polarimetric SAR imaging. Many of the details can be found in [14].

We use the convention where vectors appear in bold font e.g. $\boldsymbol{x}$ and matrices are underlined e.g. $\underline{\mathrm{A}}$.

II. Forward Model

When discussing the wave propagation for polarimetric SAR we begin with the time-harmonic Maxwell's equations:

$$\begin{aligned}
\nabla \times \boldsymbol{E}(k,\boldsymbol{x}) &= i\omega \boldsymbol{B}(k,\boldsymbol{x}) && (1)\\
\nabla \times \boldsymbol{H}(k,\boldsymbol{x}) &= \boldsymbol{J}(k,\boldsymbol{x}) - i\omega \boldsymbol{D}(k,\boldsymbol{x}) && (2)\\
\nabla \cdot \boldsymbol{D}(k,\boldsymbol{x}) &= \rho && (3)\\
\nabla \cdot \boldsymbol{B}(k,\boldsymbol{x}) &= 0 && (4)
\end{aligned}$$

where $\boldsymbol{E}$ is the electric field, $\boldsymbol{B}$ is the magnetic induction field, $\boldsymbol{D}$ is the electric displacement field, $\boldsymbol{H}$ is the magnetic intensity or magnetic field, ρ is the charge density, $\boldsymbol{J}$ is the current density, and $k = \omega/c$ where ω is the angular frequency and c the vacuum speed of light. We assume that the SAR system under consideration has two dipole antennas, a and b which travel along paths $\boldsymbol{\gamma}_a(s)$ and $\boldsymbol{\gamma}_b(s)$, where s is known as the slow time. We assume that dipole a transmits the waveform $p_a(t)$, and the scattered field is received on both a and b. Similarly dipole b transmits the waveform $p_b(t)$, and the scattered field is received on both a and b. Here t is known as the fast time. We denote the Fourier transforms of the waveforms by P_a and P_b. We also assume the dipoles have direction $\widehat{\boldsymbol{e}}_a$ and $\widehat{\boldsymbol{e}}_b$ respectively.

We model the target scene as a collection of dipoles located at various pixels and with various orientations. We denote the direction of the dipole at location $\boldsymbol{x}$ by $\widehat{\boldsymbol{e}}_T(\boldsymbol{x}) = [\cos\theta(\boldsymbol{x}), \sin\theta(\boldsymbol{x}), 0]$, where all angles θ are with respect to the x-axis as displayed in Figure (1). Similarly we model clutter as dipoles at various locations $\boldsymbol{y}$ with orientations $\widehat{\boldsymbol{e}}_C(\boldsymbol{y})$.

In the frequency domain, the far-field electric field due to a radiating dipole of length a, located at position $\boldsymbol{\gamma}_a(s)$ and pointing in direction $\widehat{\boldsymbol{e}}_a$, is [3]

$$\boldsymbol{E}_a(k,\boldsymbol{x}) = \widehat{\boldsymbol{R}}^a_{\boldsymbol{x},s} \times \left(\widehat{\boldsymbol{R}}^a_{\boldsymbol{x},s} \times \widehat{\boldsymbol{e}}_a\right) \frac{e^{ikR^a_{\boldsymbol{x},s}}}{4\pi R^a_{\boldsymbol{x},s}} F^a(k\widehat{\boldsymbol{R}}^a_{\boldsymbol{x},s}\cdot\widehat{\boldsymbol{e}}_a) P_a(k) \tag{5}$$

where $\boldsymbol{R}^a_{\boldsymbol{x},s} = \boldsymbol{x} - \boldsymbol{\gamma}_a(s)$, $R^a_{\boldsymbol{x},s} = |\boldsymbol{R}^a_{\boldsymbol{x},s}|$, and

$$F^a(k\cos\theta) = a\mathrm{sinc}\left(\frac{ka}{2}\cos\theta\right) \tag{6}$$

is the antenna pattern of the dipole a.

We assume that the dipole $\widehat{\boldsymbol{e}}_{sc}(\boldsymbol{x})$ acts as a receiving antenna with antenna pattern F^{sc}. Here we use the subscript and superscript sc to indicate a general scatterer in the scene, i.e. either target or clutter. The current induced on the dipole radiates again as a dipole antenna, and this process has strength $\rho(\boldsymbol{x})$ and again antenna pattern F^{sc}.

The measured data $D^{sc}_{a,b}$ due to scattering from $\widehat{\boldsymbol{e}}_{sc}(\boldsymbol{x})$ is the current on the receiving dipole b:

$$\begin{aligned}
&D^{sc}_{a,b}(k,s) \propto \widehat{\boldsymbol{e}}_b \cdot \boldsymbol{E}(k, \boldsymbol{\gamma}_b(s))\\
&= \int \rho(\boldsymbol{x}) \frac{e^{ik(R^a_{\boldsymbol{x},s} + R^b_{\boldsymbol{x},s})}}{16\pi^2 R^a_{\boldsymbol{x},s} R^b_{\boldsymbol{x},s}} F^{sc}(k\widehat{\boldsymbol{R}}^a_{\boldsymbol{x},s}\cdot\widehat{\boldsymbol{e}}_{sc}) F^{sc}(k\widehat{\boldsymbol{R}}^b_{\boldsymbol{x},s}\cdot\widehat{\boldsymbol{e}}_{sc})\\
&F^b(k\widehat{\boldsymbol{R}}^b_{\boldsymbol{x},s}\cdot\widehat{\boldsymbol{e}}_b) F^a(k\widehat{\boldsymbol{R}}^a_{\boldsymbol{x},s}\cdot\widehat{\boldsymbol{e}}_a) \widehat{\boldsymbol{e}}_{sc} \cdot \left[\widehat{\boldsymbol{R}}^a_{\boldsymbol{x},s} \times \left(\widehat{\boldsymbol{R}}^a_{\boldsymbol{x},s} \times \widehat{\boldsymbol{e}}_a\right)\right]\\
&\widehat{\boldsymbol{e}}_b \cdot \left[\widehat{\boldsymbol{R}}^b_{\boldsymbol{x},s} \times \left(\widehat{\boldsymbol{R}}^b_{\boldsymbol{x},s} \times \widehat{\boldsymbol{e}}_{sc}\right)\right] P_a(k)\, d\boldsymbol{x}.
\end{aligned} \tag{7}$$

Here the two subscripts on the left side of (7) indicate that we transmit on dipole a and receive on dipole b. Equation (7) also includes an integration over all possible ground locations $\boldsymbol{x}$ in the visible scene. We suppress the dependence of $\widehat{\boldsymbol{e}}_{sc}$ on $\boldsymbol{x}$ for ease of notation.

We rewrite (7) as follows. First we let $[\widehat{\boldsymbol{R}}^a_{\boldsymbol{x},s} \times (\widehat{\boldsymbol{R}}^a_{\boldsymbol{x},s} \times \widehat{\boldsymbol{e}}_a)] = (x_a, y_a, z_a)$ and $[\widehat{\boldsymbol{R}}^b_{\boldsymbol{x},s} \times (\widehat{\boldsymbol{R}}^b_{\boldsymbol{x},s} \times \widehat{\boldsymbol{e}}_b)] = (x_b, y_b, z_b)$. Now if we transmit and receive on both a and b and assume that the antennas are collocated (that is, we assume a mono-static system) we have the following expression for the data vector:

$$\begin{aligned}
\boldsymbol{D}^{sc}(k,s) &= \int e^{2ikR_{\boldsymbol{x},s}} \rho_{sc}(\boldsymbol{x}) \qquad (8)\\
&\times \begin{pmatrix} \mathcal{A}_{a,a}x_a^2 & \mathcal{A}_{a,a}x_a y_a & \mathcal{A}_{a,a}x_a y_a & \mathcal{A}_{a,a}y_a^2 \\ \mathcal{A}_{a,b}x_a x_b & \mathcal{A}_{a,b}x_a y_b & \mathcal{A}_{a,b}y_a x_b & \mathcal{A}_{a,b}y_a y_b \\ \mathcal{A}_{b,a}x_a x_b & \mathcal{A}_{b,a}y_a x_b & \mathcal{A}_{b,a}x_a y_b & \mathcal{A}_{b,a}y_b y_b \\ \mathcal{A}_{b,b}x_b^2 & \mathcal{A}_{b,b}x_b y_b & \mathcal{A}_{b,b}x_b y_b & \mathcal{A}_{b,b}y_b^2 \end{pmatrix} \boldsymbol{S}(\theta_{sc}) d\boldsymbol{x}
\end{aligned}$$

where we define

$$\begin{aligned}
\mathcal{A}_{i,j} = (1/16\pi^2 R^2_{\boldsymbol{x},s})(F^{sc}(k\widehat{\boldsymbol{R}}_{\boldsymbol{x},s}\cdot\widehat{\boldsymbol{e}}_{sc}))^2 F^i(k\widehat{\boldsymbol{R}}_{\boldsymbol{x},s}\cdot\widehat{\boldsymbol{e}}_i)\\
\times F^j(k\widehat{\boldsymbol{R}}_{\boldsymbol{x},s}\cdot\widehat{\boldsymbol{e}}_j) P_i(k)
\end{aligned} \tag{9}$$

for $i = a, b$ and $j = a, b$. We now have expressed our forward model in terms of the quantity

$$\boldsymbol{S}(\theta_{sc}) = \begin{pmatrix} \cos^2\theta_{sc} \\ \cos\theta_{sc}\sin\theta_{sc} \\ \sin\theta_{sc}\cos\theta_{sc} \\ \sin^2\theta_{sc} \end{pmatrix}. \tag{10}$$

$\boldsymbol{S}(\theta_{sc})$ is referred to as the scattering vector, or the vectorized scattering matrix, for a dipole scatterer [9], [8]. The two unknowns we wish to recover are $\rho(\boldsymbol{x})$ and $\boldsymbol{S}(\theta_{sc})$.

The model is linear in terms of ρ but nonlinear in θ_{sc}, because the argument of the radiation pattern of the scatterer, F^{sc}, contains θ_{sc}. In order to remove this nonlinearity we will make assumptions about the radiation patterns of the target and clutter [14].

A. Target Scattering Model

For an extended target, we assume that we obtain a strong return from the scatterer only when the orientation of the target is perpendicular to the look direction:

$$F^T(k\widehat{\boldsymbol{R}}^i_{\boldsymbol{x},s}\cdot\widehat{\boldsymbol{e}}_T)=\begin{cases}1 & \text{if } \widehat{\boldsymbol{R}}_{\boldsymbol{x},s}\cdot\widehat{\boldsymbol{e}}_T\approx 0\\ 0 & \text{otherwise.}\end{cases} \tag{11}$$

We change the subscript and superscript to the letter T to indicate that we are considering a target scatterer, i.e. a scatterer of interest. This assumption converts (8) to the following form:

$$\boldsymbol{D}^T(k,s)=\mathcal{F}^T[\boldsymbol{T}(\boldsymbol{x})]=\int e^{2ikR_{\boldsymbol{x},s}}\underline{A}^T(k,s,\boldsymbol{x})\boldsymbol{T}(\boldsymbol{x})d\boldsymbol{x} \tag{12}$$

where we define $\boldsymbol{T}(\boldsymbol{x})=\rho_T(\boldsymbol{x})\boldsymbol{S}(\theta_T)$ as the target function. The amplitude matrix, $\underline{A}^T$, now depends only on $\widehat{\boldsymbol{e}}_a$ and $\widehat{\boldsymbol{e}}_b$ and not $\widehat{\boldsymbol{R}}_{\boldsymbol{x},s}$.

B. Clutter Scattering Model

For clutter scatterers, we assume that the scattering is isotropic:

$$F^C(k\widehat{\boldsymbol{R}}_{\boldsymbol{x},s}\cdot\widehat{\boldsymbol{e}}_C)=1 \tag{13}$$

$\forall k,s,\boldsymbol{x}$. Thus, we obtain the following forward model for clutter data:

$$\boldsymbol{D}^C(k,s)=\mathcal{F}^C[\boldsymbol{C}](k,s)=\int e^{2ikR_{\boldsymbol{x},s}}\underline{A}^C(k,s,\boldsymbol{x})\boldsymbol{C}(\boldsymbol{x})d\boldsymbol{x}, \tag{14}$$

where we let the function that describes the clutter be $\boldsymbol{C}(\boldsymbol{x})=\rho_C(\boldsymbol{x})\boldsymbol{S}_C(\theta)$. The amplitude matrix, $\underline{A}_C$, has the form of equation (8) with the dependence on $\widehat{\boldsymbol{e}}_C$ removed.

The two forward operators $\mathcal{F}^C$ and $\mathcal{F}^T$ are different, but under the assumptions above, both are now linear operators.

C. Total Forward Model

We now can combine the target and clutter data with measurement noise $\boldsymbol{n}$ to obtain the full data model:

$$\begin{aligned}\boldsymbol{D}(k,s)&=\mathcal{F}^T[\boldsymbol{T}](k,s)+\mathcal{F}^C[\boldsymbol{C}](k,s)+\boldsymbol{n}(k,s)\\&=\boldsymbol{D}^T(k,s)+\boldsymbol{D}^C(k,s)+\boldsymbol{n}(k,s).\end{aligned} \tag{15}$$

where we assume $\boldsymbol{n}$ is a 4×1 vector. We also make the assumption now that the target vector $\boldsymbol{T}(\boldsymbol{x})$, clutter vector $\boldsymbol{C}(\boldsymbol{x})$, and noise vector $\boldsymbol{n}(k,s)$ are all second-order stationary stochastic processes.

We specify now the first- and second-order statistics for the three processes. We let $\boldsymbol{\mu}(\boldsymbol{x})$ denote the mean of the target process and we assume that $\boldsymbol{C}$ and $\boldsymbol{n}$ are zero-mean processes. In addition we denote the 4×4 covariance matrices for $\boldsymbol{T},\boldsymbol{C}$, and $\boldsymbol{n}$ by $\underline{C}^T(\boldsymbol{x},\boldsymbol{x}')$, $\underline{\mathcal{R}}^C(\boldsymbol{x},\boldsymbol{x}')$, and $\underline{\mathcal{S}}^n(s,s',k,k')$, respectively. In addition, we assume that the target, clutter, and noise are all mutually statistically independent.

III. Image Formation in the presence of noise and clutter

In order to form an image of the target, we use a filtered-backprojection-type reconstruction method [14]. Specifically we apply the backprojection operator $\mathcal{K}$ to our data to form an image $\boldsymbol{I}$ of the target, i.e.

$$\boldsymbol{I}(\boldsymbol{z})=(\mathcal{K}\boldsymbol{D})(\boldsymbol{z})=\int e^{-i2k\boldsymbol{R}_{\boldsymbol{z},s}}\underline{Q}(\boldsymbol{z},s,k)\boldsymbol{D}(k,s)dkds \tag{16}$$

where $\boldsymbol{I}(\boldsymbol{z})=[I_{a,a}(\boldsymbol{z}),I_{a,b}(\boldsymbol{z}),I_{b,a}(\boldsymbol{z}),I_{b,b}(\boldsymbol{z})]$ and where $\underline{Q}$ is a 4×4 filter matrix to be determined below.

To determine the optimal filter $\underline{Q}$, we will minimize the expected mean-square error between the reconstructed image $\boldsymbol{I}$ and the actual target function $\boldsymbol{T}$. This method seeks to minimize the effect of noise and clutter on the resulting image while preserving the strength of the target. This approach is an extension to the vector case of the work [15].

We denote by $\mathcal{E}$ the error process $\mathcal{E}(\boldsymbol{z})=\boldsymbol{I}(\boldsymbol{z})-\boldsymbol{T}(\boldsymbol{z})$; with this notation, the expected mean-square error (MSE) is

$$\mathcal{J}(\underline{Q})=\int E[|\mathcal{E}(\boldsymbol{z})|^2]d\boldsymbol{z}=\int E[(\mathcal{E}(\boldsymbol{z})^\dagger(\mathcal{E}(z))]d\boldsymbol{z}. \tag{17}$$

where $\mathcal{E}^\dagger$ denotes the complex conjugate transpose of the vector $\mathcal{E}$.

In order to minimize $\mathcal{J}(\underline{Q})$ we find the variation of $\mathcal{J}$ with respect to $\underline{Q}$. After some calculations [14], the variational minimization of $\mathcal{J}$ with respect to $\underline{Q}$ leads to the integral equation:

$$\begin{aligned}0=\Bigg(\int\overline{\eta}e^{i\boldsymbol{x}\cdot(\boldsymbol{\zeta}'-\boldsymbol{\zeta})}\Big[&(\underline{Q}\underline{A}^T\eta-\underline{\tilde{\chi}}_\Omega)(\underline{S}_T+\underline{M})(\underline{A}^T)^\dagger\\&+(\underline{Q}\underline{A}^C\eta)\underline{S}_C(\underline{A}^C)^\dagger\Big]d\boldsymbol{\zeta}'\Bigg)_{(r,k)}+(\underline{Q}\underline{\tilde{S}}^n\eta)_{(r,k)},\end{aligned} \tag{18}$$

$\forall r$ and $\forall k$, where $\underline{\tilde{\chi}}_\Omega(\boldsymbol{z},\boldsymbol{\xi})$ is a characteristic function that is smoothed to avoid ringing in the image. The matrix $\underline{M}$ is the two-dimensional Fourier transform of the quantity $\boldsymbol{\mu}(\boldsymbol{x})\boldsymbol{\mu}^\dagger(\boldsymbol{x}')$ and is related to the bias of the estimator. The spectral density functions $\underline{S}_T$ and $\underline{S}_C$ are the two-dimensional Fourier transforms of the autocovariance of the target and clutter processes.

Minimizing the variance of the error process rather than the expected mean-square error results in the same minimization as above except that the bias term $\underline{M}$ drops out. If we also make a stationarity assumption on $(\boldsymbol{T}-\boldsymbol{\mu})$ and $\boldsymbol{C}$, then we can perform the integration in equation (18) and solve for $\underline{Q}$:

$$\begin{aligned}\underline{Q}^\dagger=\Big[|\eta|^2(\underline{A}^T(\underline{S}^T)^\dagger(\underline{A}^T)^\dagger+\underline{A}^C(\underline{S}^C)^\dagger(\underline{A}^C)^\dagger)+\eta(\tilde{S}^n)^\dagger\Big]^{-1}\\\times\eta\underline{A}^T(\underline{S}^T)^\dagger\underline{\tilde{\chi}}^\dagger_\Omega.\end{aligned} \tag{19}$$

IV. Numerical Experiments

We carried out numerical experiments to verify our theory. The scene on the ground is assumed to be 50 meters by 50 meters, represented by 100 by 100 pixels. That is, our resolution cell size is .5 meter by .5 meter. We consider targets with varying orientation and we assume that $\rho_T(\boldsymbol{x}) = 1$ for all target locations $\boldsymbol{x}$. We assume the target is always twenty pixels in length and one pixel in width. For the clutter process we assume that a clutter dipole is located at every possible $\boldsymbol{x}$ in the scene of interest. All the random variables $\rho_C(\boldsymbol{x})$ are independent identically distributed (i.i.d.) Gaussian random variables with zero mean and unit complex variance. The random variables $\theta_C(\boldsymbol{x})$ are i.i.d uniform between the angles $[0, \pi/2]$. We note that in this case the clutter process $\boldsymbol{C}(\boldsymbol{x})$ is wide-sense stationary. Measurement noise is not explicitly included in the numerical simulations; this is equivalent to assuming that the data has been prewhitened. Note that although we assume the data is prewhitened we include the noise term in the expression for the filter given in Equation (19). This term serves as a regularization term as the matrix to be inverted in (19) has a high condition number. Explicitly we write it as rI where I is the 3×3 identity matrix and $r \in \mathbb{C}$ is the regularization parameter. Currently this parameter is chosen by the user but optimizing the parameter choice is future work.

The flight path is a linear one along the y axis; we take $\boldsymbol{\gamma}(s) = [x_0, s, z_0]$, where we have assumed that x_0 and z_0 are fixed. The two antennas used for transmission and reception have orientations $\widehat{\boldsymbol{e}}_a = [1, 0, 0]'$ and $\widehat{\boldsymbol{e}}_b = [0, 1, 0]'$ which are defined with respect to the origin in the scene on the ground. We may think of a as having the vertical or V orientation and b as having the horizontal or H orientation. Our frequency range is $1 - 1.5$ GHz, where we sample at a rate above Nyquist.

In producing the data, we did not use the directional scattering assumptions on the target and clutter process, (11) and (13). That is, we do not approximate the radiation patterns when simulating the data. In this way we avoid the corresponding "inverse crimes" [4]. From the simulated data, we form images of the target scattering vector, or target function, $\boldsymbol{T}(\boldsymbol{x})$ using both the standard SAR channel-by-channel image reconstruction and our coupled polarimetric reconstruction. We then compare two sets of images for each example. We also provide plots and tables that list the differences in mean-square error and the image signal-to-clutter (SCR) ratios respectively for the various cases.

1) Example One - Target Perpendicular to Flight Path: We first consider the case when the target has the orientation $\widehat{\boldsymbol{e}}_T(\boldsymbol{x}) = [1, 0, 0]'$ which is parallel to the a, or V, antenna. In Figure (2) we show the actual target scene (top) and then the target-embedded-in-clutter scene (bottom). We display the target-only data obtained using the $aa, ab,$ and bb antenna combinations for both transmission and reception in Figure (3). As expected, there is no target response in the HH and HV channels when $s = 38$, as this is the point the flight path crosses the x-axis where the target lies, and consequently the target is viewed end-on. However there is data at this point in the VV data set, because the target orientation is parallel to the V antenna and the dot products in the data therefore have value one which is the maximum. When clutter is present the target data is completely obscured.

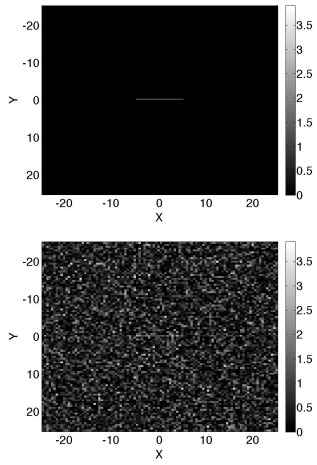

Fig. 2. VV component of target vector and target plus clutter vector, target perpendicular to flight path, note X and Y are in meters

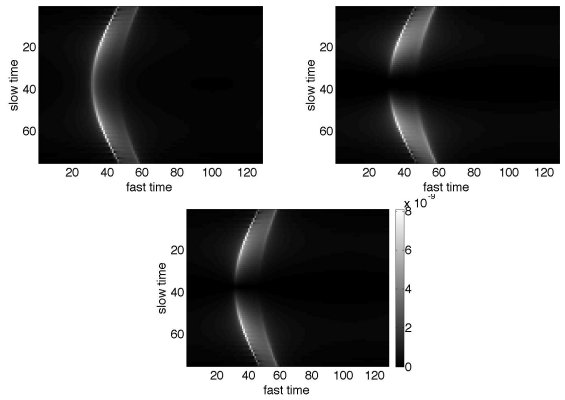

Fig. 3. VV, HH, and HV target-only data for the case of a target perpendicular to the flight path and parallel to the V antenna

We present the results of the standard image reconstruction in Figure (4) (top) and our coupled reconstruction (bottom). Note the image color scale corresponds to the reflectivity or scattering strength, this is inherently a dimensionless quantity. Here we only show the result of the VV image as the other two images are flat as expected. In this case we have signal-to-clutter ratio of 10dB. Note that the image is significantly more focused in the coupled reconstruction case. We plot the signal-to-clutter ratio versus the mean-square error in Figure (5). The MSE is reduced by an order of magnitude with the coupled reconstruction technique. This is noteworthy because the filter used here was obtained by minimizing the variance of the error process and not the MSE.

Lastly we display the image signal-to-clutter ratio in Table (4.1). We calculate image SCR by performing the reconstruction techniques on target-only data and clutter-only data and

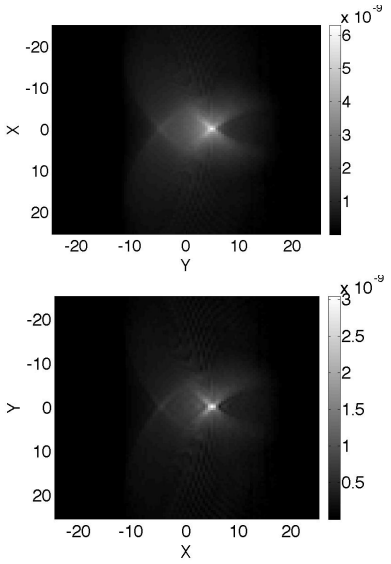

Fig. 4. VV images formed using the standard vs. coupled reconstruction

then compare the energy in each set of images. Here we see a significant improvement in the image SCR; this is clear from the images themselves.

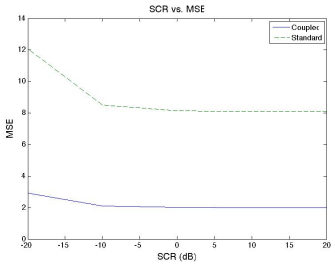

Fig. 5. SCR vs. MSE for the standard and coupled images respectively, target perpendicular to flight path

Scene SCR	Image SCR (standard)	Image SCR (coupled)
-20	0.3122	.7869
-10	0.9873	2.4884
0	3.1223	7.8691
10	9.8735	24.8844
20	31.2226	78.6912

TABLE I

SCENE SCR IN DB AND STANDARD VS. COUPLED IMAGE SCR IN DB, TARGET PERPENDICULAR TO FLIGHT PATH

2) Example Two - Target at $45\,^\circ$*:* Our second example considers the case when the target has orientation $\widehat{e}_T = [1/\sqrt{2}, 1/\sqrt{2}, 0]'$. In this case we expect the coupled technique to aid even more in target reconstruction as there is more information to be gained by using all three data sets. In Figure (6) we show the true target scene. Next we display the target-only HV data in Figure (7); the HH and VV data are almost identical. We see in this case that the target is not visible

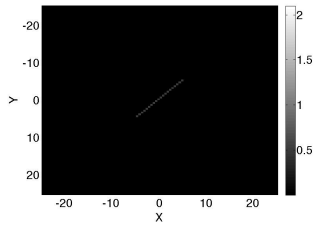

Fig. 6. HV component of target vector, $45\,^\circ$ polarized target

for most of the flight path. However there is data in all three channels so we expect to see some improvement by using our coupled reconstruction.

Next we display example images formed using the two different techniques. Here we show only the result of the HV image as the other two images are almost identical. These are shown in Figure (8). In this case we have signal-to-clutter ratio of 20dB. We observe that both algorithms struggle to reconstruct the target, because the data contains very little target information. In addition looking at Figure (7) we see that the target is only visible for first ten or so slow time values. This is due to the fact that the target is significantly closer to the antenna during this portion of the flight path. This data obscures data resulting from a majority of the target leading to the poor reconstruction. There are clearly artifacts visible in Figure (8). The effects are partially due to edge effects and also due to choice of the regularization parameter. We have seen significant reduction in these artifacts by decreasing the regularization parameter, however this change in the parameter value leads to a change in the reconstructed target orientation. We note that in Figure (8) our coupled scheme is able to properly display the orientation of the target while the standard reconstruction fails in this respect.

Next we plot the mean-square error versus SCR in Figure (9). Our scheme improves the MSE only slightly because the amount of data available for reconstruction is minimal in all channels. We note however that the MSE may improve further with a change in regularization parameter.

Lastly we calculate the image SCR for each type of image and display the results in Table (4.2). We again see improvement in image SCR. As expected, the gain for coupled processing is slight because of the lack of data.

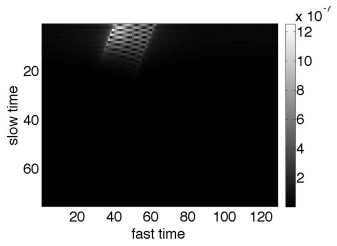

Fig. 7. HV data, target at $45\,^\circ$

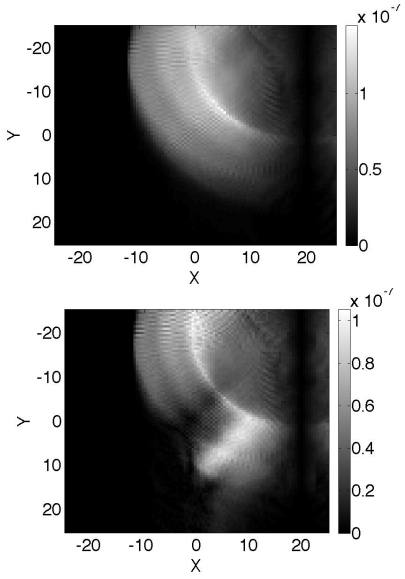

Fig. 8. HV images formed using the standard vs. coupled reconstruction

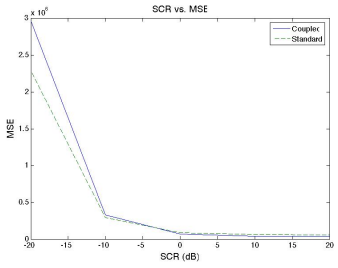

Fig. 9. SCR vs. MSE for the standard and coupled images respectively, 45° polarized target

V. Conclusion

In this work we developed a novel polarimetric imaging technique. This technique not only demonstrates how to incorporate statistical knowledge into the imaging scheme, but also demonstrates a way in which to utilize the additional information a polarimetric radar provides. We have demonstrated that our coupled reconstruction improves the image mean-square error and signal-to-clutter ratio. In addition, this method appears to be extremely useful when the target is not parallel to either of the antennas used for transmission and reception. In this case standard polarimetric techniques fail to correctly display the orientation of the target, whereas the polarimetric coupled reconstruction is able to recover this information. This work suggests that polarimetric radar may prove useful in improving SAR images and target detection capabilities. While in this work we have considered an extremely simplified target model the positive results suggest the need for further work on more complicated target scenarios. To go beyond curves and consider more complicated targets the forward model will likely need to be modified and we leave this as future work. In addition the case of multiple targets is left as future work.

Scene SCR	Image SCR (standard)	Image SCR (coupled)
-20	0.1646	0.1858
-10	0.5039	0.5069
0	1.5934	1.6031
10	5.0389	5.0694
20	15.9344	16.0308

TABLE II

Initial SCR in dB and Final Standard vs. Coupled Processing Image SCR in dB, 45° polarized target

Acknowledgment

The authors would like to thank Dr. Matthew Ferrara, Dr. Richard Albanese, and Dr. Gerald Benitz for their assistance in formulating this forward problem and inversion scheme. This work was supported by the ATR Center at AFRL[1] under contract FA8650-08-C-1322, the GAANN fellowship, the National Research Council Postdoctoral Research Associateship program, the Air Force Office of Scientific Research[1] under contract FA9550-09-1-0013 and the National Science Foundation under grant CCF-08030672.

References

[1] M.R. Allen and L.E. Hoff, "Wide-angle wideband SAR matched filter image formation for enhanced detection performance," in *SPIE Proceedings on Algorithms for Synthetic Aperture Radar Imagery*, Vol. 2230, pp: 302-314, 1994.

[2] W.M. Boerner, M.B. El-Arini, C.Y. Chan, and P.M. Mastoris, "Polarization Dependence in Electromagnetic Inverse Problems," IEEE Trans. on Antennas and Propagation, Vol. 29, No. 2, 1981.

[3] M. Cheney and B. Borden, *Fundamentals of Radar Imaging*, SIAM, Philadelphia, 2009.

[4] D. Colton and R. Kress, *Integral Equation Methods in Scattering Theory*, John Wiley and Sons, Inc., New York, 1983.

[5] R.L. Dilsavor and R.L. Moses, "Fully-Polarimetric GLRTs for Detecting Scattering Centers with Unknown Amplitude, Phase, and Tilt Angle in Terrain Clutter," in *SPIE's International Symposium on Optical Engineering in Aerospace Sensing*, Orlando, FL, 1994.

[6] E. Ertin and L.C. Potter, "Polarimetric Classification of Scattering Centers using M-ary Bayesian Decision Rules," IEEE Trans. on Aerospace and Electronic Systems, Vol. 36, No. 3, 2000.

[7] M. Gustafsson, "Multi-static synthetic aperture radar and inverse scattering," Technical Report LUTEDX, TEAT-7123, 2004.

[8] I. Hajnsek, "Inversion of Surface Parameters using Polarimetric SAR," DLR, Oberpfaffenhofen, Germany, DLR Res. Rep. FB 2001-30, 2001.

[9] J.R. Huynen, "Phenomenological Theory of Radar Targets," Ph.D. Thesis, University of Technology, Delft, The Netherlands, 1970.

[10] J.S. Lee and E. Pottier, *Polarimetric radar imaging*, Taylor and Francis, Boca Raton, 2009.

[11] L.M. Novak, M.C. Burl, and W.W. Irving, "Optimal Polarimetric Processing for Enhanced Target Detection," IEEE Trans. on Aerospace and Electronic Systems, Vol. 29, No. 1, 1993.

[12] H. Mott, *Antennas for Radar and Communications: A Polarimetric Approach*, John Wiley and Sons, Inc., New York, 1992.

[13] K. Voccola, "Statistical and Analytical Techniques in Synthetic Aperture Radar Imaging," Ph.D. Thesis, Dept. Math. Sciences, Rensselaer Polytechnic Institute, Troy, NY, 2011.

[14] B. Yazici, M. Cheney, and C.E. Yarman, "Synthetic-Aperture Inversion in the Presence of Noise and Clutter," Inverse Problems, Vol. 22, pp: 1705-1729, 2006.

[1]Consequently, the US Government is authorized to reproduce and distribute reprints for governmental purposes notwithstanding any copyright notation thereon. The views and conclusions contained herein are those of the authors and should not be interpreted as necessarily representing the official policies or endorsements, either expressed or implied, of the Air Force Research Laboratory or the US Government.